

# Enhancement of Second-Order Non-Hermitian Skin Effect by Magnetic Fields

Chang-An Li,<sup>1</sup> Björn Trauzettel,<sup>1</sup> Titus Neupert,<sup>2</sup> and Song-Bo Zhang<sup>3,2,\*</sup>

<sup>1</sup>*Institute for Theoretical Physics and Astrophysics,  
University of Würzburg, 97074 Würzburg, Germany*

<sup>2</sup>*Department of Physics, University of Zürich, Winterthurerstrasse 190, 8057, Zürich, Switzerland*

<sup>3</sup>*International Center for Quantum Design of Functional Materials (ICQD),  
Hefei National Research Center for Physical Sciences at the Microscale,  
University of Science and Technology of China, Hefei, Anhui 230026, China*

(Dated: October 10, 2023)

The non-Hermitian skin effect is a unique phenomenon in which an extensive number of eigenstates are localized at the boundaries of a non-Hermitian system. Recent studies show that the non-Hermitian skin effect is significantly suppressed by magnetic fields. In contrast, we demonstrate that the second-order skin effect (SOSE) is robust and can even be enhanced by magnetic fields. Remarkably, SOSE can also be induced by magnetic fields from a trivial non-Hermitian system that does not experience any skin effect at zero field. These properties are intimately related to the persistence and emergence of topological line gaps in the complex energy spectrum in presence of magnetic fields. Moreover, we show that a magnetic field can drive a non-Hermitian system from a hybrid skin effect, where the first-order skin effect and SOSE coexist, to pure SOSE. Our results describe a qualitatively new magnetic field behavior of the non-Hermitian skin effect.

*Introduction.*—Non-Hermitian physics appears in a variety of physical systems in quantum optics, ultracold atoms, and condensed matter [1–4]. In recent years, many unique non-Hermitian phenomena have been revealed, which show no counterparts in their Hermitian limit [5–31]. One prime example is the non-Hermitian skin effect (NHSE), an anomalous localization of extensive eigenstates at the open boundaries of a non-Hermitian system [5–11]. This intriguing phenomenon has triggered intense research interests both theoretically and experimentally [5–12, 32–71]. In the conventional (first-order) NHSE, the skin modes are localized at  $(d-1)$  or lower dimensional boundaries, and importantly, their number scales with the volume  $L^d$ , where  $d$  and  $L$  are dimension and linear size of the system, respectively [72]. Recently, NHSE has been generalized to higher ( $n$ -th) orders with certain constraints on the geometry, where the skin modes are localized to  $(d-n)$  or lower dimensional boundaries and their number scales as  $L^{d-n}$  with  $2 \leq n \leq d$  [72–74]. Notably, SOSE (with  $n=2$ ) has been predicted in several lattice models and implemented in several experimental platforms [72–82].

In presence of uniform magnetic fields, charged particles display localization behavior due to cyclotron motion in the plane perpendicular to the field [83, 84]. Hence, the magnetic field tends to localize most particles in the bulk of the system in contrast to NHSE. It is thus interesting to investigate the coexistence of NHSE and magnetic fields. So far, research efforts have been mostly dedicated to the first-order skin effect (FOSE) with the outcome that it is significantly suppressed even by small magnetic fields due to competing tendencies of localization [85–87]. However, as we show below, this physical picture does not apply to the higher-order NHSE.

In this work, we study systematically the influence of

magnetic fields on SOSE in two dimensions (2D). Remarkably, we find that SOSE is not suppressed but rather enhanced by magnetic fields. It can even be induced by magnetic fields in otherwise trivial non-Hermitian systems without any skin effect. We explain such anomalous behaviors by topological properties of the complex energy spectrum. We demonstrate the results on several prototypical non-Hermitian models for SOSE with line-gap or point-gap topology. In the latter case, we further show a magnetic field-driven transition from a hybrid skin effect with coexistence of FOSE and SOSE to pure SOSE. Finally, we discuss feasible experimental platforms to test our predictions.

*Phenomenology of SOSE and its magnetic robustness.*—To better illustrate our results, we first consider 2D non-Hermitian systems in which FOSE is absent but SOSE can be present. The absence of FOSE is achieved by imposing certain spatial symmetries to the bulk of the system, such as mirror and inversion symmetries, together with an appropriate choice of open boundary conditions (OBC) [88]. SOSE in the non-Hermitian system usually arises as a consequence of the interplay between 1D edge modes and local non-reciprocity [72, 73]. Note that the spatial symmetries are locally violated at the boundary. If the system has edge modes along the boundary with OBC in one direction and periodic boundary conditions (PBC) in the other direction, these edge modes will experience non-reciprocity. Thus, upon further imposing OBC to the other direction, they evolve into skin corner modes (SCMs) [Fig. 1(a)]. The number of SCMs scales with the linear system size  $\sim \mathcal{O}(L)$ , as inherited from the edge modes. This is the hallmark of SOSE [72].

The properties of SOSE in this case depend substantially on the edge modes, which can be of topologi-

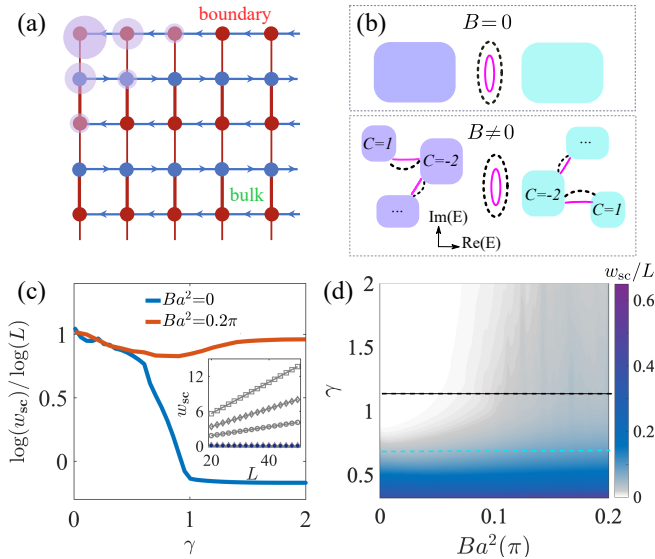


Fig. 1. (a) Schematic of the model in Eq. (2) with OBC in  $x$ - and  $y$ -directions. The red thick and thin bonds indicate dimerized hoppings in  $y$ -direction; the blue arrow lines indicate non-reciprocal hoppings in  $x$ -direction, and the purple dots mark the SCMs. (b) Sketch of the energy spectrum (colored boxes) in absence (top) and presence (bottom) of a magnetic field. Solid (dashed) lines indicate the spectrum of SCMs (edge modes). (c)  $\log(w_{sc})/\log(L)$  at  $Ba^2 = 0$  (blue) and  $0.2\pi$  (orange) as a function of  $\gamma$  for  $L = 160$  and  $\xi = 30$ , respectively. Inset: skin corner weight  $w_{sc}$  as a function of  $L$  at  $B = 0$  for  $\xi = 1$ ,  $\gamma = 0.4, 0.5, 0.6, 1.0$  and  $1.6$  (from top to bottom). (d)  $w_{sc}/L$  as a function of  $\gamma$  and  $B$  for  $L = 60$ .  $\lambda = 1$  for (c,d).

cal origin. Similar to the Hermitian case, the edge modes are typically protected by bulk gaps, referred to as line gaps in the non-Hermitian context [14, 32, 89]. Indeed, we observe a coincidence between the appearance/disappearance of SOSE and line-gap transitions. The line-gap topology persists under the application of magnetic fields [Fig. 1(b)]. Thus, the robustness of SOSE based on edge modes relates to a line-gap protection. Furthermore, under strong magnetic fields, each bulk continuum spectral area generally splits into multiple non-Hermitian Hofstadter bands [lower panel in Fig. 1(b)]. Chiral edge modes appear to connect the Hofstadter bands with different Chern numbers when OBC are applied in one direction. Due to the local non-reciprocity at the boundary, these emerging edge modes likewise evolve into SCMs when OBC are further imposed in the other direction. Thus, the system exhibits enhanced SOSE due to magnetic fields.

In non-Hermitian systems with point-gap topology, we can observe the occurrence of a hybrid skin effect, where FOSE and SOSE coexist. Applying a magnetic field significantly suppresses FOSE, while it enhances SOSE [90]. As a result, the system transforms from the hybrid skin effect at zero field to pure SOSE state at strong fields.

We illustrate these intriguing behaviors within explicit models below [cf. Eqs. (2) and (3)].

*Skin corner weight.*—To quantitatively characterize SOSE under OBC, we introduce the skin corner weight  $w_{sc}$  defined as

$$w_{sc} \equiv \sum_{n, \mathbf{r}, \mathbf{r}_c} |\psi_n^R(\mathbf{r})|^4 \exp(-|\mathbf{r} - \mathbf{r}_c|/\xi), \quad (1)$$

where the sums run over all eigenstates indexed by  $n$ , lattice sites  $\mathbf{r}$ , and corner positions  $\mathbf{r}_c$ .  $\psi_n^R(\mathbf{r})$  is the right eigen wavefunction of the Hamiltonian [91].  $w_{sc}$  in Eq. (1) contains two important factors. The first factor  $|\psi_n^R(\mathbf{r})|^4$  measures the localization strength of eigenstates. With only this factor,  $w_{sc}$  reduces to the inverse participation ratio which characterizes the localization properties of the whole system. The second factor  $\exp(-|\mathbf{r} - \mathbf{r}_c|/\xi)$ , which decays exponentially away from the corners with decay length  $\xi$ , selects only the modes localized at the corners. Note that  $\xi$  should be chosen much smaller than the linear system size, i.e.,  $\xi \ll L$ . For SOSE,  $w_{sc}$  is finite and scales linearly with  $L$  in 2D [92]. We can apply a power-law scaling  $w_{sc} \propto L^\alpha$  to characterize  $w_{sc}$  and extract the scaling exponent  $\alpha$ . Thus,  $\alpha = 1$  is expected for 2D systems with pure SOSE.

*Minimal model for SOSE.*—To illustrate the essential physics, we first consider a 2D minimal model for SOSE on a square lattice with two sublattices [72]. The Hamiltonian in momentum space reads

$$H(\mathbf{k}) = \lambda \sin k_y \sigma_1 + (\gamma + \lambda \cos k_y) \sigma_2 + \lambda \sin k_x \sigma_3 - i(\gamma + \lambda \cos k_x), \quad (2)$$

where  $\mathbf{k} = (k_x, k_y)$  is the wavevector,  $\lambda$  and  $\gamma$  are real parameters, and  $\{\sigma_1, \sigma_2, \sigma_3\}$  are Pauli matrices in sublattice space. We set the lattice constant to  $a = 1$ . The model features dimerized reciprocal hopping along  $y$ -direction and opposite non-reciprocal hopping for the two sublattices along  $x$ -direction [Fig. 1(a)]. The bulk energy spectrum covers finite areas in the complex plane, which indicates a geometry-dependent FOSE [63]. However, the model respects transpose-mirror symmetries in  $x$ - and  $y$ -directions, as indicated by  $\sigma_1 H^T(\mathbf{k}) \sigma_1 = H(-k_x, k_y)$  and  $\sigma_3 H^T(\mathbf{k}) \sigma_3 = H(k_x, -k_y)$ , respectively. The spectrum for any given  $k_x$  (or  $k_y$ ) consists of two open arcs with no interior in the complex plane [93]. Thus, FOSE is absent in a rectangular geometry with OBC in  $x$ - and  $y$ -directions, as we confirm numerically below [72, 93].

The appearance of SOSE in the model can be understood as follows. In absence of hopping along  $x$ -direction, the model decouples into identical Su-Schrieffer-Heeger chains along  $y$ -direction. Under OBC in  $y$ -direction, localized edge modes appear in the parameter regime  $|\gamma| < |\lambda|$ . When the non-reciprocal hoppings along  $x$ -direction are turned on, they cancel out effectively due to the transpose-mirror symmetries [Fig. 1(a)]. However, the hopping along  $x$ -direction remains locally non-reciprocal

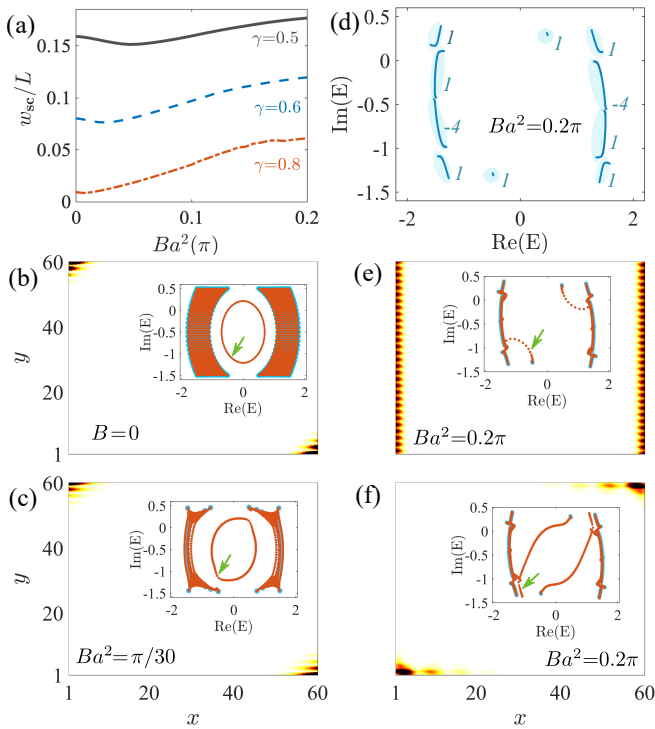


Fig. 2. (a)  $w_{sc}/L$  as a function of  $B$  for  $\xi = 1$  at different  $\gamma$ . (b)  $|\psi^R(\mathbf{r})|^2$  of a SCM at  $B = 0$  under OBC. Inset: energy spectra under PBC (cyan) and OBC (orange), respectively. The arrow marks the mode energy  $E = -0.46 - 1.03i$ . (c) The same as (b) but at  $Ba^2 = \pi/30$ . The arrow marks the mode energy  $E = -0.53 - 1.10i$ . (d) Energy spectrum at  $Ba^2 = 0.2\pi$  under PBC. The Chern numbers of the Hofstadter bands are indicated. (e)  $|\psi^R(\mathbf{r})|^2$  of an edge mode at  $Ba^2 = 0.2\pi$  under PBC (OBC) in  $y(x)$ -direction. The arrow marks the mode energy  $E = -0.68 - 0.96i$ . (f)  $|\psi^R(\mathbf{r})|^2$  of a corner mode at  $Ba^2 = 0.2\pi$  under OBC. Insets in (e-f): the corresponding energy spectra. The arrow marks the mode energy  $E = -1.16 - 1.19i$ .  $\gamma = 0.5$  in (b-f) and other parameters are  $L = 60$ ,  $\lambda = 1$ .

at the boundaries, since the transpose-mirror symmetries are locally violated there. Thus, when OBC are imposed in both directions, the edge modes evolve into SCMs, leading to SOSE. In the other regime  $|\gamma| \geq |\lambda|$ , there are no edge modes and thus no SOSE. These features are confirmed numerically by  $w_{sc}$  in Fig. 1(c). Clearly,  $w_{sc}$  is finite and increases monotonically with decreasing  $\gamma$  for  $|\gamma| < |\lambda|$ , while it is negligibly small for  $|\gamma| \geq |\lambda|$  [Fig. 1(c), inset]. Figure 1(c) illustrates  $\log(w_{sc})/\log(L)$  as a function of  $\gamma$  [94]. We find that  $\log(w_{sc})/\log(L)$  is a negative constant for  $|\gamma| \geq |\lambda|$ , whereas it saturates quickly to 1 as  $\gamma$  decreases for  $|\gamma| < |\lambda|$ . Thus, we observe the expected behavior of  $w_{sc}$  to properly characterize SOSE.

**Magnetic robustness and enhancement of SOSE.**— Now, we apply a magnetic field  $B$  to the system and study how it affects SOSE. Without loss of generality, we adopt the Landau gauge  $\mathbf{A} = (-By, 0, 0)$ . Figures 1(d) and 2(a) display  $w_{sc}$  as a function of  $B$  for different

$\gamma$ . Strikingly,  $w_{sc}$  is not really suppressed by  $B$  for any  $|\gamma| < |\lambda|$ . Instead, it remains approximately a constant for small  $B$  and increases significantly as  $B$  increases. This indicates that SOSE is robust and becomes even more pronounced under magnetic fields, in stark contrast to FOSE [85–87].

To better understand the line-gap protection behind the magnetic robustness and enhancement, we analyze the energy spectrum of the system. At zero field, the bulk spectrum consists of two detached bands separated by a line gap [Fig. 2(b), inset]. In a ribbon geometry along  $x$ -direction, there are edge modes with energies lying in the line gap when  $|\gamma| < |\lambda|$  [93], forming a closed loop with point-gap topology in the complex-energy plane. They evolve into SCMs when further imposing OBC in  $x$ -direction [Fig. 2(b)]. Note that these features are present as long as the line gap persists in the bulk spectrum. When gradually applying a magnetic field, the bulk spectrum changes adiabatically, while keeping the line gap open [Fig. 2(c)]. Therefore, SOSE stays robust against magnetic fields. Notably, the line gap closes at  $|\gamma| = |\lambda|$  and reopens for  $|\gamma| > |\lambda|$ , indicating a topological phase transition. Consequently, SOSE disappears for  $|\gamma| > |\lambda|$ . In this sense, the robustness of SOSE is protected by a nontrivial line gap in the bulk spectrum.

With increasing  $B$ , the two bulk bands evolve into multiple non-Hermitian Hofstadter bands [95] that are well separated by line gaps [Fig. 2(d)]. We find that each Hofstadter band carries a nonzero Chern number [93, 96]. When OBC are applied in either direction, edge modes emerge, which connect one Hofstadter band to another with different Chern numbers [Fig. 2(e)]. These edge modes evolve to SCMs when we impose OBC in both directions [Fig. 2(f)]. Notably, the line gaps separating different Hofstadter bands remain over a broad range of  $B$ , as can be seen in the corresponding Hofstadter spectra [93]. This results in more pronounced SOSE under magnetic fields.

**SOSE induced by magnetic fields.**— We demonstrate that SOSE can even be induced by a magnetic field in the regime  $|\gamma| \geq |\lambda|$ . At  $B = 0$ , the system has nearly the same energy spectrum under different boundary conditions [Fig. 3(a)]. Accordingly, it does not have SCMs under OBC. However, in presence of  $B$ , the boundary spectrum under OBC becomes substantially different from that under partial PBC [Fig. 3(b), inset]. In particular, under OBC, we observe eigenstates whose energies strongly deviate from both bulk and edge spectra. In fact, these eigenstates correspond to SCMs [Fig. 3(b)]. Their number is proportional to  $L$ , as indicated by the corresponding  $w_{sc}/L$  in Fig. 3(c) and the scaling exponent  $\alpha$  in Fig. 1(c) at finite  $B$ . From Fig. 3(d) [also Fig. 1(d)], it is clear that  $w_{sc}/L$  increases monotonically from 0 at  $B = 0$  to significant values ( $w_{sc}/L \gtrsim 0.01$ ) at  $Ba^2 \simeq 0.1\pi$  for any  $|\gamma| \geq |\lambda|$ . These observations demonstrate that SOSE can be induced by magnetic fields.

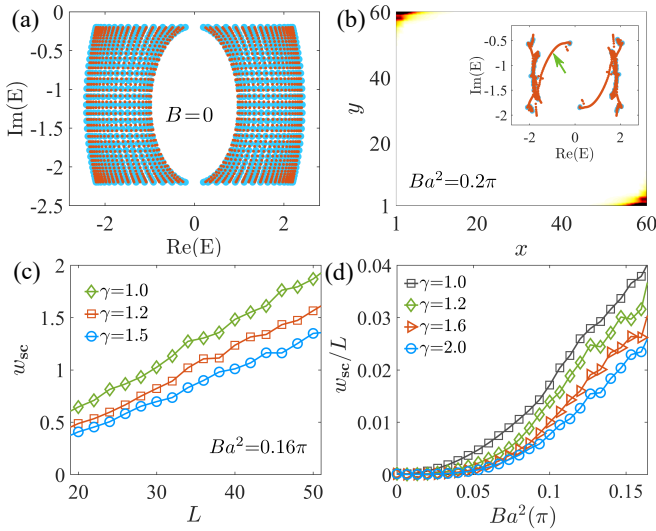


Fig. 3. (a) Energy spectra at  $B = 0$  under OBC (orange) and PBC (cyan), respectively. (b)  $|\psi^R(\mathbf{r})|^2$  of a SCM at  $Ba^2 = 0.2\pi$  under OBC. Inset: the corresponding energy spectrum. The arrow marks the mode energy  $E = -1.00 - 0.73i$ . (c)  $w_{sc}$  as a function of  $L$  at  $Ba^2 = 0.16\pi$  for different  $\gamma \geq 1$ . (d)  $w_{sc}/L$  as a function of  $Ba^2$  for  $\gamma \geq 1$ .  $L = 60$  for (a,b,d),  $\gamma = 1.2$  for (a,b) and other parameters are  $\lambda = 1$  and  $\xi = 1$ .

It is noteworthy that the field-induced SOSE is always associated with the formation of non-Hermitian Hofstadter bands with nonzero Chern numbers in the bulk spectrum [Fig. 3(b), inset]. This indicates that the induced SOSE can also be understood from the emergence of topological line gaps: the chiral-like edge modes in the line gaps evolve into SCMs by the local non-reciprocity under OBC.

*Transition from hybrid skin effect to pure SOSE.*— Finally, we show that a hybrid skin effect can emerge in non-Hermitian systems with point-gap topology, and the system transforms from the hybrid skin effect to pure SOSE by applying magnetic fields. To be specific, we consider the model [74, 75]

$$\mathcal{H}(\mathbf{k}) = M(\mathbf{k})\tau_0 + i\chi(\sin k_y\tau_x + \sin k_x\tau_y) - \mathbf{h} \cdot \boldsymbol{\tau}, \quad (3)$$

where  $M(\mathbf{k}) = -t(\cos k_x + \cos k_y)$ ,  $\mathbf{h} = (h_x, h_y)$ , and  $\boldsymbol{\tau} = (\tau_x, \tau_y)$ .  $t$ ,  $\chi$  and  $\mathbf{h}$  are real parameters. At zero field, the PBC spectrum has point-gap topology and encloses a finite area [93]. Previous studies identified SOSE in this model, consistent with the point-gap topology [74, 75]. Remarkably, we find that FOSE appears simultaneously, leading to a hybrid skin effect. SOSE generates  $\mathcal{O}(L)$  corner modes in the energy regimes associated with intrinsic second-order topology [dashed circles in Fig. 4(a)] [74], while FOSE generates  $\mathcal{O}(L^2)$  corner modes outside those regimes [93]. The hybrid skin effect is also corroborated by the scaling exponent  $\alpha$ , which is significantly larger than 1 (the value for pure SOSE) [97].

In Fig. 4, we track the evolution of energies and wave-

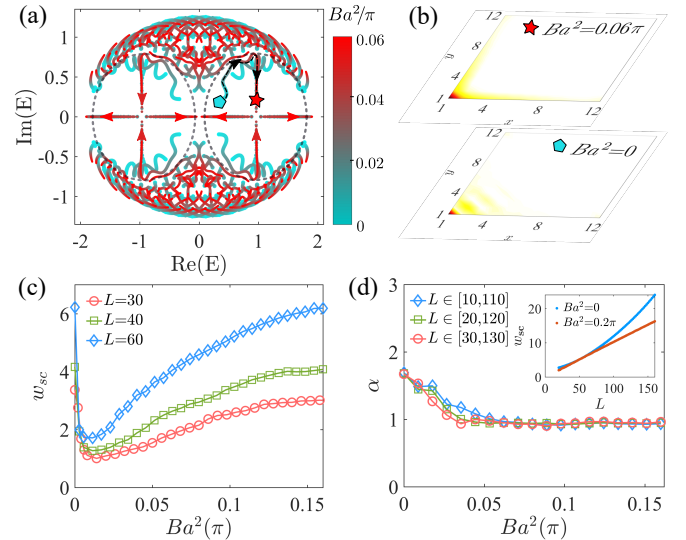


Fig. 4. (a) Flow of the OBC spectrum of Eq. (3) as  $Ba^2$  increases from 0 (cyan) to  $0.06\pi$  (red). (b)  $|\psi^R(\mathbf{r})|^2$  of a SCM at  $Ba^2 = 0$  and  $0.06\pi$ , respectively. (c)  $w_{sc}$  as a function of  $Ba^2$  for  $L = 30, 40$  and  $60$ , respectively. (d)  $\alpha$  as a function of  $Ba^2$ , extracted by fitting  $w_{sc}(L) \propto L^\alpha$  with  $L \in [10, 100]$ ,  $[20, 110]$  and  $[30, 130]$ , respectively. Inset:  $w_{sc}$  as a function of  $L$  at  $Ba^2 = 0$  and  $0.2\pi$ , respectively.  $L = 12$  in (a,b) and other parameters are  $t = \chi = 1$ ,  $h_x = h_y = 0.1$ , and  $\xi = 1$ .

functions of the SCMs associated with SOSE, as the magnetic field  $B$  increases from zero to a finite value. Clearly, they stay inside the original energy regimes while gradually moving towards the real axis, as illustrated by red arrows in Fig. 4(a). Notably, they remain well-localized at the corners during this process [Fig. 4(b)]. These features again show the magnetic robustness of the SCMs associated with SOSE.

With increasing  $B$ , the system transforms gradually from the hybrid skin effect to pure SOSE. To demonstrate this, we plot  $w_{sc}$  as a function of  $B$  in Fig. 4(c). For small  $B$ ,  $w_{sc}$  drops suddenly to a finite value, indicating the strong suppression of FOSE [85–87]. As  $B$  further increases,  $w_{sc}$  grows gradually, indicating the enhancement of SOSE [93]. In Fig. 4(d), we plot  $\alpha$  with increasing  $B$ . Strikingly,  $\alpha$  drops to a plateau at 1, which is faster for larger  $L$ . The scaling behavior of  $w_{sc}$  with respect to  $L$  changes from a curved line at zero field to a straight line at strong fields [Fig. 4(d), inset]. These observations strongly support the transition to pure SOSE. From a bulk perspective, the magnetic field drives the energy spectrum with only point gaps to one with non-Hermitian Hofstadter bands separated by line gaps [93].

*Discussion and conclusion.*—To summarize, we have presented a comprehensive description of the influence of magnetic fields on SOSE. We have shown that magnetic fields enhance and induce SOSE in non-Hermitian systems. We have also revealed a magnetic field-driven transition from a hybrid skin effect to pure SOSE in

non-Hermitian systems with point-gap topology. Such anomalous magnetic robustness and enhancement of SOSE stem from the persistence and emergence of topological line gaps in the bulk energy spectrum.

Our results can be verified by other models endowed with SOSE, and generalized to the third-order skin effect [93]. Our predictions can be tested in different physical platforms such as ultracold atoms, electric circuits and acoustic systems [78–80, 98, 99]. Notably, SOSE has been realized in electric circuits recently [79, 80]. Desired effective magnetic fields can be obtained by inserting a uniform synthetic magnetic flux into the circuits [100]. In ultracold-atom systems, NHSE have also been observed [98]. Highly tunable gauge fields in this platform have been achieved through lattice shading [101] and laser-assisted tunneling [102, 103].

We thank J. Budich and T. Bzdušek for valuable discussion. C.A.L. thanks the University of Zurich for hospitality at the early stage of this work. This work was supported by the SFB1170 “ToCoTronics”, the Würzburg-Dresden Cluster of Excellence ct.qmat, EXC2147, Project-id 390858490, and the High Tech Agenda Bayern, the European Research Council (ERC) under the European Union’s Horizon 2020 research and innovation program (ERC-StG-Neupert-757867-PARATOP). S.B.Z was also supported by the UZH Postdoc Grant.

---

\* songbo.zhang@physik.uzh.ch

- [1] C. M. Bender, “Making sense of non-Hermitian Hamiltonians”, *Rep. Prog. Phys.* **70**, 947 (2007).
- [2] R. El-Ganainy, K. G. Makris, M. Khajavikhan, Z. H. Musslimani, S. Rotter, and D. N. Christodoulides, “Non-Hermitian physics and PT symmetry”, *Nat. Phys.* **14**, 11 (2018).
- [3] Y. Ashida, Z. Gong, and M. Ueda, “Non-Hermitian physics”, *Adv. Phys.* **69**, 249 (2020).
- [4] E. J. Bergholtz, J. C. Budich, and F. K. Kunst, “Exceptional topology of non-Hermitian systems”, *Rev. Mod. Phys.* **93**, 015005 (2021).
- [5] T. E. Lee, “Anomalous edge state in a non-Hermitian lattice”, *Phys. Rev. Lett.* **116**, 133903 (2016).
- [6] S. Yao and Z. Wang, “Edge states and topological invariants of non-Hermitian systems”, *Phys. Rev. Lett.* **121**, 086803 (2018).
- [7] F. K. Kunst, E. Edvardsson, J. C. Budich, and E. J. Bergholtz, “Biorthogonal bulk-boundary correspondence in non-Hermitian systems”, *Phys. Rev. Lett.* **121**, 026808 (2018).
- [8] K. Zhang, Z. Yang, and C. Fang, “Correspondence between winding numbers and skin modes in non-Hermitian systems”, *Phys. Rev. Lett.* **125**, 126402 (2020).
- [9] N. Okuma, K. Kawabata, K. Shiozaki, and M. Sato, “Topological origin of non-Hermitian skin effects”, *Phys. Rev. Lett.* **124**, 086801 (2020).
- [10] X. Zhang, T. Zhang, M.-H. Lu, and Y.-F. Chen, “A review on non-Hermitian skin effect”, *Advances in Physics: X* **7**, 2109431 (2022).
- [11] N. Okuma and M. Sato, “Non-Hermitian topological phenomena: A review”, *Annu. Rev. Condens. Matter Phys.* **14**, 83 (2023).
- [12] S. Yao, F. Song, and Z. Wang, “Non-Hermitian chern bands”, *Phys. Rev. Lett.* **121**, 136802 (2018).
- [13] Z. Gong, Y. Ashida, K. Kawabata, K. Takasan, S. Higashikawa, and M. Ueda, “Topological phases of non-Hermitian systems”, *Phys. Rev. X* **8**, 031079 (2018).
- [14] H. Shen, B. Zhen, and L. Fu, “Topological band theory for non-Hermitian Hamiltonians”, *Phys. Rev. Lett.* **120**, 146402 (2018).
- [15] K. Esaki, M. Sato, K. Hasebe, and M. Kohmoto, “Edge states and topological phases in non-Hermitian systems”, *Phys. Rev. B* **84**, 205128 (2011).
- [16] D. Leykam, K. Y. Bliokh, C. Huang, Y. D. Chong, and F. Nori, “Edge modes, degeneracies, and topological numbers in non-Hermitian systems”, *Phys. Rev. Lett.* **118**, 040401 (2017).
- [17] S. Lieu, “Topological phases in the non-Hermitian Su-Schrieffer-Heeger model”, *Phys. Rev. B* **97**, 045106 (2018).
- [18] Y. Xiong, “Why does bulk boundary correspondence fail in some non-Hermitian topological models”, *Journal of Physics Communications* **2**, 035043 (2018).
- [19] C. Yin, H. Jiang, L. Li, R. Lü, and S. Chen, “Geometrical meaning of winding number and its characterization of topological phases in one-dimensional chiral non-Hermitian systems”, *Phys. Rev. A* **97**, 052115 (2018).
- [20] V. M. Martinez Alvarez, J. E. Barrios Vargas, and L. E. F. Foa Torres, “Non-Hermitian robust edge states in one dimension: Anomalous localization and eigenspace condensation at exceptional points”, *Phys. Rev. B* **97**, 121401 (2018).
- [21] K. Kawabata, T. Bessho, and M. Sato, “Classification of exceptional points and non-Hermitian topological semimetals”, *Phys. Rev. Lett.* **123**, 066405 (2019).
- [22] K. Yokomizo and S. Murakami, “Non-bloch band theory of non-Hermitian systems”, *Phys. Rev. Lett.* **123**, 066404 (2019).
- [23] H. Zhou and J. Y. Lee, “Periodic table for topological bands with non-Hermitian symmetries”, *Phys. Rev. B* **99**, 235112 (2019).
- [24] J. Y. Lee, J. Ahn, H. Zhou, and A. Vishwanath, “Topological correspondence between Hermitian and non-Hermitian systems: Anomalous dynamics”, *Phys. Rev. Lett.* **123**, 206404 (2019).
- [25] W. B. Rui, M. M. Hirschmann, and A. P. Schnyder, “ $\mathcal{PT}$ -symmetric non-Hermitian Dirac semimetals”, *Phys. Rev. B* **100**, 245116 (2019).
- [26] R. Okugawa and T. Yokoyama, “Topological exceptional surfaces in non-Hermitian systems with parity-time and parity-particle-hole symmetries”, *Phys. Rev. B* **99**, 041202 (2019).
- [27] J. C. Budich and E. J. Bergholtz, “Non-Hermitian topological sensors”, *Phys. Rev. Lett.* **125**, 180403 (2020).
- [28] H. Hu and E. Zhao, “Knots and non-Hermitian bloch bands”, *Phys. Rev. Lett.* **126**, 010401 (2021).
- [29] C. C. Wojcik, X.-Q. Sun, T. Bzdušek, and S. Fan, “Homotopy characterization of non-Hermitian Hamiltonians”, *Phys. Rev. B* **101**, 205417 (2020).
- [30] V. Kornich and B. Trauzettel, “Andreev bound states in junctions formed by conventional and  $\mathcal{PT}$ -symmetric non-Hermitian superconductors”, *Phys. Rev. Res.* **4**,

- 033201 (2022).
- [31] S.-B. Zhang, M. M. Denner, T. Bzdušek, M. A. Sentef, and T. Neupert, “Symmetry breaking and spectral structure of the interacting Hatano-Nelson model”, *Phys. Rev. B* **106**, L121102 (2022).
- [32] K. Kawabata, K. Shiozaki, M. Ueda, and M. Sato, “Symmetry and topology in non-Hermitian physics”, *Phys. Rev. X* **9**, 041015 (2019).
- [33] M. Ezawa, “Non-Hermitian higher-order topological states in nonreciprocal and reciprocal systems with their electric-circuit realization”, *Phys. Rev. B* **99**, 201411 (2019).
- [34] T. Liu, Y.-R. Zhang, Q. Ai, Z. Gong, K. Kawabata, M. Ueda, and F. Nori, “Second-order topological phases in non-Hermitian systems”, *Phys. Rev. Lett.* **122**, 076801 (2019).
- [35] C. H. Lee and R. Thomale, “Anatomy of skin modes and topology in non-Hermitian systems”, *Phys. Rev. B* **99**, 201103 (2019).
- [36] S. Longhi, “Topological phase transition in non-Hermitian quasicrystals”, *Phys. Rev. Lett.* **122**, 237601 (2019).
- [37] X.-W. Luo and C. Zhang, “Higher-order topological corner states induced by gain and loss”, *Phys. Rev. Lett.* **123**, 073601 (2019).
- [38] K.-I. Imura and Y. Takane, “Generalized bulk-edge correspondence for non-Hermitian topological systems”, *Phys. Rev. B* **100**, 165430 (2019).
- [39] L. Jin and Z. Song, “Bulk-boundary correspondence in a non-Hermitian system in one dimension with chiral inversion symmetry”, *Phys. Rev. B* **99**, 081103 (2019).
- [40] L. Herviou, J. H. Bardarson, and N. Regnault, “Defining a bulk-edge correspondence for non-Hermitian Hamiltonians via singular-value decomposition”, *Phys. Rev. A* **99**, 052118 (2019).
- [41] D.-W. Zhang, L.-Z. Tang, L.-J. Lang, H. Yan, and S.-L. Zhu, “Non-Hermitian topological Anderson insulators”, *Sci. China Phys., Mech. & Astron.* **63**, 267062 (2020).
- [42] L. Xiao, T. Deng, K. Wang, G. Zhu, Z. Wang, W. Yi, and P. Xue, “Non-Hermitian bulk-boundary correspondence in quantum dynamics”, *Nat. Phys.* **16**, 761 (2020).
- [43] L. Li, C. H. Lee, and J. Gong, “Topological switch for non-Hermitian skin effect in cold-atom systems with loss”, *Phys. Rev. Lett.* **124**, 250402 (2020).
- [44] T. Hofmann, T. Helbig, F. Schindler, N. Salgo, M. Brzezińska, M. Greiter, *et al.*, “Reciprocal skin effect and its realization in a topoelectrical circuit”, *Phys. Rev. Res.* **2**, 023265 (2020).
- [45] N. Matsumoto, K. Kawabata, Y. Ashida, S. Furukawa, and M. Ueda, “Continuous phase transition without gap closing in non-Hermitian quantum many-body systems”, *Phys. Rev. Lett.* **125**, 260601 (2020).
- [46] L. Li, C. H. Lee, S. Mu, and J. Gong, “Critical non-Hermitian skin effect”, *Nat. Commun.* **11**, 5491 (2020).
- [47] P. Gao, M. Willatzen, and J. Christensen, “Anomalous topological edge states in non-Hermitian piezophononic media”, *Phys. Rev. Lett.* **125**, 206402 (2020).
- [48] A. Ghatak, M. Brandenbouer, J. V. Wezel, and C. Coulais, “Observation of non-Hermitian topology and its bulk-edge correspondence in an active mechanical metamaterial”, *Proc. Natl. Ac. Sc. U.S.A.* **117**, 29561 (2020).
- [49] Z. Yang, K. Zhang, C. Fang, and J. Hu, “Non-Hermitian bulk-boundary correspondence and auxiliary generalized brillouin zone theory”, *Phys. Rev. Lett.* **125**, 226402 (2020).
- [50] T. Helbig, T. Hofmann, S. Imhof, M. Abdelghany, T. Kiessling, L. W. Molenkamp, C. H. Lee, A. Szameit, M. Greiter, and R. Thomale, “Generalized bulk-boundary correspondence in non-Hermitian topoelectrical circuits”, *Nat. Phys.* **16**, 747 (2020).
- [51] K. Yokomizo and S. Murakami, “Topological semimetal phase with exceptional points in one-dimensional non-Hermitian systems”, *Phys. Rev. Res.* **2**, 043045 (2020).
- [52] M. M. Denner, A. Skurativska, F. Schindler, M. H. Fischer, R. Thomale, T. Bzdušek, and T. Neupert, “Exceptional topological insulators”, *Nat. Commun.* **12**, 5681 (2021).
- [53] N. Okuma and M. Sato, “Quantum anomaly, non-Hermitian skin effects, and entanglement entropy in open systems”, *Phys. Rev. B* **103**, 085428 (2021).
- [54] H.-G. Zirnstein, G. Refael, and B. Rosenow, “Bulk-boundary correspondence for non-Hermitian Hamiltonians via green functions”, *Phys. Rev. Lett.* **126**, 216407 (2021).
- [55] T. Haga, M. Nakagawa, R. Hamazaki, and M. Ueda, “Liouvillian skin effect: Slowing down of relaxation processes without gap closing”, *Phys. Rev. Lett.* **127**, 070402 (2021).
- [56] J. Claes and T. L. Hughes, “Skin effect and winding number in disordered non-Hermitian systems”, *Phys. Rev. B* **103**, L140201 (2021).
- [57] C.-X. Guo, C.-H. Liu, X.-M. Zhao, Y. Liu, and S. Chen, “Exact solution of non-Hermitian systems with generalized boundary conditions: Size-dependent boundary effect and fragility of the skin effect”, *Phys. Rev. Lett.* **127**, 116801 (2021).
- [58] K.-M. Kim and M. J. Park, “Disorder-driven phase transition in the second-order non-Hermitian skin effect”, *Phys. Rev. B* **104**, L121101 (2021).
- [59] F. Schindler and A. Prem, “Dislocation non-Hermitian skin effect”, *Phys. Rev. B* **104**, L161106 (2021).
- [60] K. Yokomizo and S. Murakami, “Scaling rule for the critical non-Hermitian skin effect”, *Phys. Rev. B* **104**, 165117 (2021).
- [61] X.-Q. Sun, P. Zhu, and T. L. Hughes, “Geometric response and disclination-induced skin effects in non-Hermitian systems”, *Phys. Rev. Lett.* **127**, 066401 (2021).
- [62] D. Wu, J. Xie, Y. Zhou, and J. An, “Connections between the open-boundary spectrum and the generalized brillouin zone in non-Hermitian systems”, *Phys. Rev. B* **105**, 045422 (2022).
- [63] K. Zhang, Z. Yang, and C. Fang, “Universal non-Hermitian skin effect in two and higher dimensions”, *Nat. Commun.* **13**, 2496 (2022).
- [64] F. Alsallom, L. Herviou, O. V. Yazyev, and M. Brzezińska, “Fate of the non-Hermitian skin effect in many-body fermionic systems”, *Phys. Rev. Res.* **4**, 033122 (2022).
- [65] S. Franca, V. Könye, F. Hassler, J. van den Brink, and C. Fulga, “Non-Hermitian physics without gain or loss: The skin effect of reflected waves”, *Phys. Rev. Lett.* **129**, 086601 (2022).
- [66] F. Qin, R. Shen, and C. H. Lee, “Non-Hermitian squeezed polarons”, *Phys. Rev. A* **107**, L010202 (2023).
- [67] W.-T. Xue, Y.-M. Hu, F. Song, and Z. Wang, “Non-Hermitian edge burst”, *Phys. Rev. Lett.* **128**, 120401 (2022).

- (2022).
- [68] K. Suthar, Y. Wang, Y. P. Huang, H. H. Jen, and J. S. You, “Non-Hermitian many-body localization with open boundaries”, *Phys. Rev. B* **106**, 064208 (2022).
- [69] L. Jezequel and P. Delplace, “Non-Hermitian spectral flows and Berry-Chern monopoles”, *Phys. Rev. Lett.* **130**, 066601 (2023).
- [70] Y. Wang, K. Suthar, H. H. He, Y. T. Hsu, and J. S. You, “Non-Hermitian skin effects on many-body localized and thermal phases”, arXiv:2210.12998.
- [71] Y. Tanaka, R. Takahashi, and R. Okugawa, “Nonsymmorphic-symmetry-enforced non-Hermitian skin effects”, arXiv:2306.08923.
- [72] K. Kawabata, M. Sato, and K. Shiozaki, “Higher-order non-Hermitian skin effect”, *Phys. Rev. B* **102**, 205118 (2020).
- [73] C. H. Lee, L. Li, and J. Gong, “Hybrid higher-order skin-topological modes in nonreciprocal systems”, *Phys. Rev. Lett.* **123**, 016805 (2019).
- [74] R. Okugawa, R. Takahashi, and K. Yokomizo, “Second-order topological non-Hermitian skin effects”, *Phys. Rev. B* **102**, 241202 (2020).
- [75] R. Okugawa, R. Takahashi, and K. Yokomizo, “Non-Hermitian band topology with generalized inversion symmetry”, *Phys. Rev. B* **103**, 205205 (2021).
- [76] Y. Fu, J. Hu, and S. Wan, “Non-Hermitian second-order skin and topological modes”, *Phys. Rev. B* **103**, 045420 (2021).
- [77] Y. Li, C. Liang, C. Wang, C. Lu, and Y.-C. Liu, “Gain-loss-induced hybrid skin-topological effect”, *Phys. Rev. Lett.* **128**, 223903 (2022).
- [78] X. Zhang, Y. Tian, J.-H. Jiang, M.-H. Lu, and Y.-F. Chen, “Observation of higher-order non-Hermitian skin effect”, *Nat. Commun.* **12**, 5377 (2021).
- [79] L. S. Palacios, S. Tchoumakov, M. Guix, I. Pagonabarraga, S. Sánchez, and A. G. Grushin, “Guided accumulation of active particles by topological design of a second-order skin effect”, *Nat. Commun.* **12**, 4691 (2021).
- [80] D. Zou, T. Chen, W. He, J. Bao, C. H. Lee, H. Sun, and X. Zhang, “Observation of hybrid higher-order skin-topological effect in non-Hermitian topoelectrical circuits”, *Nat. Commun.* **12**, 7201 (2021).
- [81] W. Zhu and J. Gong, “Hybrid skin-topological modes without asymmetric couplings”, *Phys. Rev. B* **106**, 035425 (2022).
- [82] C. Shang, S. Liu, R. Shao, P. Han, X. Zang, X. Zhang, *et al.*, “Experimental identification of the second-order non-Hermitian skin effect with physics-graph-informed machine learning”, *Advanced Science* **9**, 2202922 (2022).
- [83] K. v. Klitzing, G. Dorda, and M. Pepper, “New method for high-accuracy determination of the fine-structure constant based on quantized Hall resistance”, *Phys. Rev. Lett.* **45**, 494 (1980).
- [84] M. E. Cage, K. Klitzing, A. Chang, F. Duncan, M. Haldane, R. B. Laughlin, A. Pruisken, and D. Thouless, *The quantum Hall effect* (Springer Science & Business Media, 2012).
- [85] N. Okuma and M. Sato, “Topological phase transition driven by infinitesimal instability: Majorana fermions in non-Hermitian spintronics”, *Phys. Rev. Lett.* **123**, 097701 (2019).
- [86] M. Lu, X.-X. Yan, and M. Franz, “Magnetic suppression of non-Hermitian skin effects”, *Phys. Rev. Lett.* **127**, 256402 (2021).
- [87] K. Shao, Z.-T. Cai, H. Geng, W. Chen, and D. Y. Xing, “Cyclotron quantization and mirror-time transition on nonreciprocal lattices”, *Phys. Rev. B* **106**, L081402 (2022).
- [88] When the bulk spectrum covers finite areas in the complex plane, FOSE may be geometry-dependent [63] and appear when OBC are imposed to a particular direction. These symmetries can enforce degeneracy of eigenenergies, preventing point-gap topology in the complex bulk energy spectrum in specific directions. Thus, FOSE is forbidden when OBC are applied to the corresponding directions.
- [89] D. S. Borgnia, A. J. Kruchkov, and R.-J. Slager, “Non-Hermitian boundary modes and topology”, *Phys. Rev. Lett.* **124**, 056802 (2020).
- [90] It is worth noting that line gaps develop quickly under the application of magnetic fields [see Fig. S6 in the Supplemental Material (SM) [93]].
- [91] The skin corner weight  $w_{sc}$  remains the same if we use alternatively the left eigenstate  $\psi_n^L(\mathbf{r})$ .
- [92] FOSE (if present) also features skin corner modes and contribute to  $w_{sc}$  when the system boundaries are not perfectly aligned with the direction of the non-reciprocal hopping. However, in this case,  $w_{sc}$  scales quadratically with  $L$ , as we have verified in the SM.
- [93] See Supplemental Material at [URL to be added by publisher] for details of (Sec. S1) absence of point-gap topology under symmetry constraints, (Sec. S2) non-Hermitian Hofstadter bands, (Sec. S3) Chern numbers of non-Hermitian Hofstadter bands, (Sec. S4) evolution of the energy spectrum at small fields, (Sec. S5) edge spectrum of the models on a ribbon geometry, (Sec. S6) SOSE model with point gap topology, (Sec. S7) generalization to other models with SOSE, (Sec. S8) magnetic suppression of FOSE, and (Sec. S9) magnetic robustness of the third-order skin effect, which include Refs. [12, 14, 34, 63, 72, 73, 80, 81, 85–87, 96, 104, 105].
- [94] Note that  $\log(w_{sc})/\log(L)$  becomes equivalent to the scaling exponent  $\alpha$  when  $L$  and  $\xi$  are much larger than the localization length of the SCMs.
- [95] D. R. Hofstadter, “Energy levels and wave functions of Bloch electrons in rational and irrational magnetic fields”, *Phys. Rev. B* **14**, 2239 (1976).
- [96] Y. Hatsugai, T. Fukui, and H. Aoki, “Topological analysis of the quantum Hall effect in graphene: Dirac-fermi transition across van Hove singularities and edge versus bulk quantum numbers”, *Phys. Rev. B* **74**, 205414 (2006).
- [97] The scaling exponent  $\alpha \rightarrow 2$  in the thermodynamic limit as FOSE modes scale with  $\mathcal{O}(L^2)$  and dominate  $w_{sc}$  in the thermodynamic limit. This is confirmed by our numerical result that  $\alpha$  increases as  $L$  grows [93].
- [98] Q. Liang, D. Xie, Z. Dong, H. Li, H. Li, B. Gadway, W. Yi, and B. Yan, “Dynamic signatures of non-Hermitian skin effect and topology in ultracold atoms”, *Phys. Rev. Lett.* **129**, 070401 (2022).
- [99] L. Zhang, Y. Yang, Y. Ge, Y.-J. Guan, Q. Chen, Q. Yan, *et al.*, “Acoustic non-Hermitian skin effect from twisted winding topology”, *Nat. Commun.* **12**, 6297 (2021).
- [100] S. Li, X.-X. Yan, J.-H. Gao, and Y. Hu, “Circuit quantum electrodynamics simulator of the two-dimensional Su-Schrieffer-Heeger model: higher-order topological phase transition induced by a continuously varying mag-

- netic field”, *Opt. Express* **30**, 17054 (2022).
- [101] P. Hauke, O. Tieleman, A. Celi, C. Ölschläger, J. Simonet, J. Struck, *et al.*, “Non-abelian gauge fields and topological insulators in shaken optical lattices”, *Phys. Rev. Lett.* **109**, 145301 (2012).
- [102] H. Miyake, G. A. Siviloglou, C. J. Kennedy, W. C. Burton, and W. Ketterle, “Realizing the harper Hamiltonian with laser-assisted tunneling in optical lattices”, *Phys. Rev. Lett.* **111**, 185302 (2013).
- [103] M. Aidelsburger, M. Atala, M. Lohse, J. T. Barreiro, B. Paredes, and I. Bloch, “Realization of the Hofstadter Hamiltonian with ultracold atoms in optical lattices”, *Phys. Rev. Lett.* **111**, 185301 (2013).
- [104] W. A. Benalcazar, B. A. Bernevig, and T. L. Hughes, “Electric multipole moments, topological multipole moment pumping, and chiral hinge states in crystalline insulators”, *Phys. Rev. B* **96**, 245115 (2017).
- [105] W. A. Benalcazar, B. A. Bernevig, and T. L. Hughes, “Quantized electric multipole insulators”, *Science* **357**, 61 (2017).

## Supplemental material for “Enhancement of Second-Order Non-Hermitian Skin Effect by Magnetic Fields ”

### Appendix S1: Absence of point-gap topology under symmetry constraints

In this section, we prove the absence of point-gap topology for the minimal model in Eq. (2) in the main text [see also Eq. (S1.3)] from symmetry constraints. The model has finite areas in the bulk energy spectrum and thus may exhibit FOSE. However, the FOSE is geometry-dependent. It is absent due to vanishing winding numbers when open boundary conditions (OBC) are imposed in  $x$ - and  $y$ -directions, which we show below. For a 2D non-Hermitian Hamiltonian  $H(\mathbf{k})$ , the winding number in  $s = x/y$  direction can be defined as

$$w_s \equiv \frac{1}{2\pi i} \int_0^{2\pi} dk_s \partial_{k_s} \log \det[H(\mathbf{k})]. \quad (\text{S1.1})$$

Certain symmetry constraints are able to vanish the winding number, thus precluding the FOSE. Here, we consider the transpose-associated mirror symmetry which acts on  $H(\mathbf{k})$  as

$$M_s H^T(\mathbf{k}) M_s^{-1} = H(g_s \mathbf{k}), \quad (\text{S1.2})$$

where  $M_s$  and  $T$  indicate the mirror and transpose operations, respectively. Explicitly, the group operation  $g_s$  works as  $g_x \mathbf{k} = (-k_x, k_y)$  and  $g_y \mathbf{k} = (k_x, -k_y)$ . For the minimal model

$$H(\mathbf{k}) = \lambda \sin k_y \sigma_1 + (\gamma + \lambda \cos k_y) \sigma_2 + \lambda \sin k_x \sigma_z - i(\gamma + \lambda \cos k_x), \quad (\text{S1.3})$$

the corresponding transpose operations are  $M_x = \sigma_1$  and  $M_y = \sigma_3$ . When  $M_x$  symmetry is preserved, we find that

$$\begin{aligned} w_x &= \frac{1}{2\pi i} \int_{-\pi}^{\pi} dk_x \partial_{k_x} \log \det[H(k_x, k_y)] \\ &= \frac{1}{2\pi i} \int_{-\pi}^{\pi} dk_x \partial_{k_x} \log \det[M_x H^T(-k_x, k_y) M_x^{-1}] \\ &= \frac{1}{2\pi i} \int_{-\pi}^{\pi} dk_x \partial_{k_x} \log \det[H(-k_x, k_y)] \\ &= \frac{1}{2\pi i} \int_{\pi}^{-\pi} d(-k_x) \partial_{-k_x} \log \det[H(k_x, k_y)] \\ &= -w_x. \end{aligned} \quad (\text{S1.4})$$

Therefore,  $w_x = 0$ . Similarly, we find  $w_y = 0$  when  $M_y$  is present.

Intuitively, we find that because of the transpose-mirror symmetry, the states with  $(k_x, k_y)$  and  $(-k_x, k_y)$  must be degenerate in energy. Thus, for any given  $k_x$  (or  $k_y$ ), the spectrum consists of two open arcs with no interior in the complex plane, as shown in Figs. S1(a) and (b). As a result, there is no FOSE when OBCs are imposed in  $x$ - and  $y$ -directions. In contrast, for given  $k_x \pm k_y$ , we find that in general, the spectrum consists of two loops with point gaps in the complex energy plane. This result indicates that the FOSE will appear when OBC are instead imposed in the diagonal directions (i.e.,  $[11]$  and  $[1\bar{1}]$  directions).



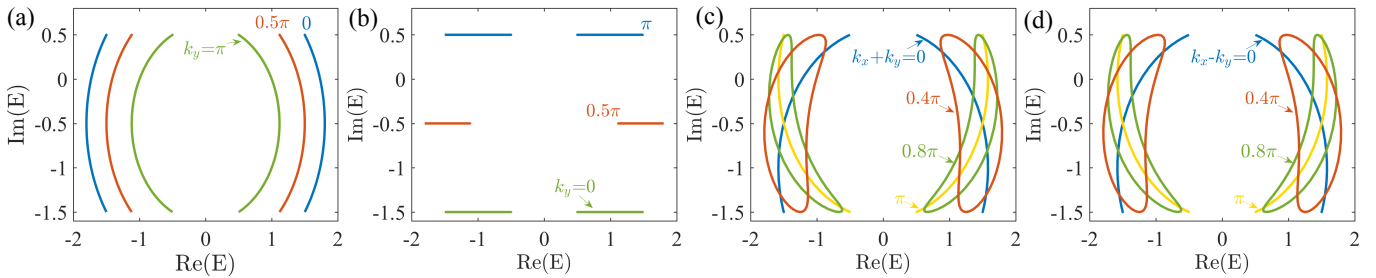


Fig. S1. (a) Energy spectrum for given  $k_y$ . For any  $k_y$ , the spectrum consists of two open arcs with no interior in the complex plane. (b) the same as (a) but for given  $k_x$ . (c) Energy spectrum for given  $k_x + k_y$ . In general, the spectrum for a given  $k_x + k_y$  consists of two loops in the complex plane except for  $k_x + k_y = 0$  and  $\pi$ . (d) the same as (c) but for given  $k_x - k_y$ .

## Appendix S2: Non-Hermitian Hofstadter bands

In this section, we present the non-Hermitian Hofstadter bands under strong magnetic fields. To better illustrate the Hofstadter spectrum in complex energy space, we first derive the Hamiltonian for the minimal model in Eq. (S1.3) in momentum space when the magnetic flux threading per plaquette is  $\phi \equiv Ba^2 = 2\pi p/q$ , where  $p$  and  $q$  are mutually prime integers. We label the unit cell as  $\mathbf{R} = j_x \hat{e}_x + j_y \hat{e}_y$ , where  $\hat{e}_x$  ( $\hat{e}_y$ ) is the lattice vector and  $j_x$  ( $j_y$ ) is an integer. We employ the vector potential  $\mathbf{A} = (0, Bx, 0)$  for the magnetic field  $B$ . It is convenient to introduce a proper magnetic unit cell such that the Hamiltonian can be written as

$$H = \int_0^{2\pi/q} \frac{dk_x}{2\pi/q} \int_0^{2\pi} \frac{dk_y}{2\pi} \mathbf{c}^\dagger(\mathbf{k}) h(\mathbf{k}) \mathbf{c}(\mathbf{k}), \quad (\text{S2.1})$$

where  $\mathbf{c}^\dagger(\mathbf{k})$  is a  $2q$ -component vector  $\mathbf{c}^\dagger(\mathbf{k}) = [c_{1a}^\dagger(\mathbf{k}), c_{1b}^\dagger(\mathbf{k}), c_{1a}^\dagger(\mathbf{k}), c_{2b}^\dagger(\mathbf{k}), \dots, c_{qa}^\dagger(\mathbf{k}), c_{qb}^\dagger(\mathbf{k})]$ ;  $h(\mathbf{k})$  is a matrix of  $2q$ -dimensions. We can rewrite the Hamiltonian as [96]

$$h(\mathbf{k}) = \begin{pmatrix} d_1(\mathbf{k}) & f^- & 0 & \dots & f^+ e^{+iqk_x} \\ f^+ & d_2(\mathbf{k}) & f^- & \dots & 0 \\ 0 & f^+ & \ddots & \ddots & \vdots \\ \vdots & \vdots & \ddots & d_{q-1}(\mathbf{k}) & f^- \\ f^- e^{-iqk_x} & 0 & \dots & f^+ & d_q(\mathbf{k}) \end{pmatrix}, \quad (\text{S2.2})$$

where

$$d_{j=1:q}(\mathbf{k}) = \begin{pmatrix} -i\gamma & -i\gamma e^{-i\phi j} - i\lambda e^{+ik_y} e^{+i\phi j} \\ i\gamma e^{+i\phi j} + i\lambda e^{-ik_y} e^{-i\phi j} & -i\gamma \end{pmatrix}, \quad (\text{S2.3})$$

and

$$f^+ = \begin{pmatrix} -i\lambda & 0 \\ 0 & 0 \end{pmatrix}, \quad f^- = \begin{pmatrix} 0 & 0 \\ 0 & -i\lambda \end{pmatrix}. \quad (\text{S2.4})$$

The magnetic field splits the continuum bulk bands to multiple non-Hermitian Hofstadter bands with nonzero Chern numbers. To determine the fractal structure, i.e., the number of Hofstadter bands at specific magnetic flux  $\phi \equiv Ba^2 = 2\pi p/q$  (with  $p$  and  $q$  being coprime integers and in units of the flux quantum  $h/e$ ), we need to consider the real and imaginary parts of the spectrum in the complex plane simultaneously. Let us focus on the main cases with  $p/q = 1/N$ , with  $N$  being an integer. We find that for even  $N$ , there are always  $N$  Hofstadter bands. For instance, at  $p/q = 1/6$ , there are totally 6 Hofstadter bands, as shown in Figs. S2(a) and (b). Whereas for odd  $N$ , the number of Hofstadter bands is either  $2N$  [Fig. S2(c)] or  $N + 1$  [Fig. S2(d)]. For instance, when  $N = 5(15)$ , there are 10(16) Hofstadter bands. We attribute this particular property to a shifted ‘‘chiral symmetry’’ which requires the eigenenergies to come in pairs as  $(E + i\gamma, -E + i\gamma)$ . Therefore, the number of Hofstadter bands has to be even.

We next show Hofstadter bands developed under strong magnetic fields. Figures S3(a) and (b) are typical Hofstadter spectra that display the real and imaginary parts of the bulk spectrum as functions of rational magnetic flux  $\phi$ , respectively. Saliiently, we find that fractal structures appear in the real and imaginary Hofstadter spectra

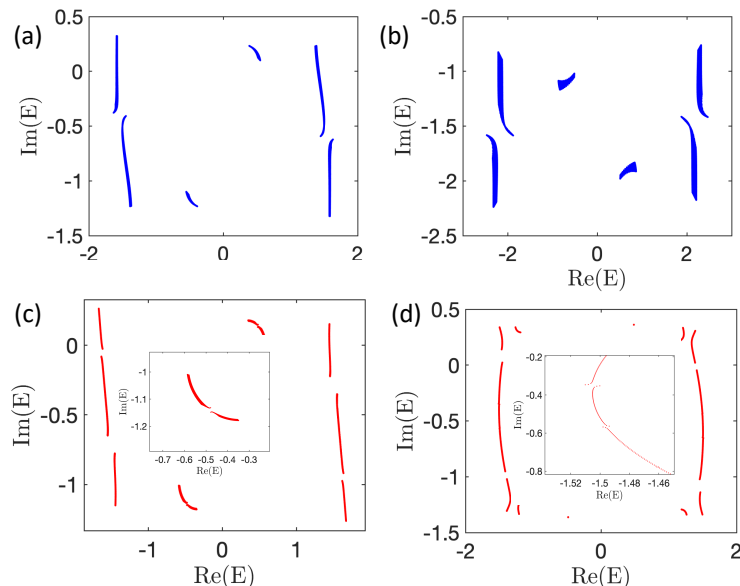


Fig. S2. Energy spectrum for given magnetic flux  $p/q = 1/6$  for (a) and (b),  $p/q = 1/5$  for (c), and  $p/q = 1/15$  for (d). Other parameters:  $\gamma = 0.5$  in (a,c,d), and  $\gamma = 1.5$  in (b). The flux is in units of the flux quantum  $h/e$ .

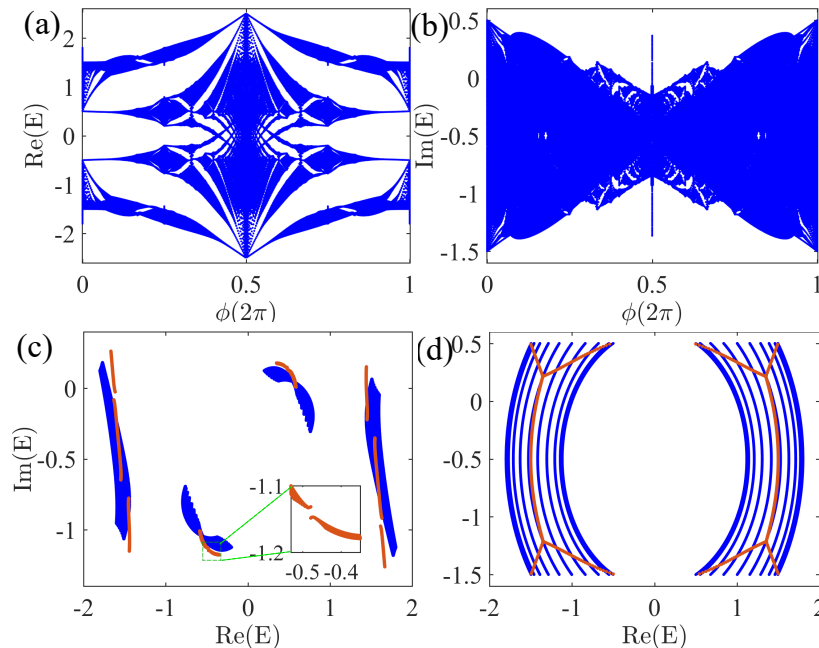


Fig. S3. (a) and (b): Real and imaginary parts of the Hofstadter spectrum, respectively. Two extra large bulk gaps appear and persist in the broad ranges [i.e.,  $(0, \pi)$  and  $(\pi, 2\pi)$ ] of  $\phi$ , as seen in (a). (c) Energy spectra at  $\phi = 2\pi/5$  (orange) and  $2\pi/4$  (blue), respectively. (d) Energy spectra at  $\phi = 0$  (blue) and  $2\pi/400$  (orange), respectively. Other parameters:  $\gamma = 0.5$ ,  $\lambda = 1$ .

independently. Large line gaps emerge and persist in a broad range of  $\phi$ . This feature indicates the emergence of separated Hofstadter bands and accounts for the robustness and enhancement of the SOSE under magnetic fields, as discussed above. The number of Hofstadter bands is determined by the value of rational flux  $\phi$  [see Fig. S3(c)], which is similar as discussed above.

Moreover, we observe striking peaks in the Hofstadter spectrum at some specific flux values. These peaks reflect a high sensitivity of the bulk spectrum to a small change of the magnetic field. The spectral sensitivity against magnetic flux grows as the linear system size  $L$  increases. For example, at  $B = 0$ , the bulk spectrum fills finite areas in the

complex plane. When we apply a small field, for instance,  $Ba^2 = 2\pi/400$  to the system, the bulk spectrum collapses to two line segments maintaining the line gap [Fig. S3(d)]. Note that a finite area in the bulk spectrum indicates the presence of a geometry-dependent FOSE [63]. This strong suppression of spectrum area by small fields is related to the magnetic suppression of the FOSE, consistent with previous works[85–87]. Similar behavior occurs at other fluxes with small values of  $q$ . We emphasize that the drastic change of Hofstadter bands and resulting anomalous peaks in the Hofstadter spectrum are absent in the Hermitian limit.

### Appendix S3: Chern numbers of non-Hermitian Hofstadter bands

In this section, we calculate the Chern numbers of the non-Hermitian Hofstadter bands. For a Hofstadter band indexed by  $n$ , the Chern number can be calculated as [12, 14, 73]

$$C_n = \frac{1}{2\pi} \iint dk_x dk_y [\partial_{k_x} A_{k_y}^n - \partial_{k_y} A_{k_x}^n], \quad (\text{S3.1})$$

where the Berry connection is defined as

$$A_{\alpha=k_x, k_y}^n \equiv \frac{\langle \psi_n^R(\mathbf{k}) | i\partial_\alpha | \psi_n^R(\mathbf{k}) \rangle}{\langle \psi_n^R(\mathbf{k}) | \psi_n^R(\mathbf{k}) \rangle} \quad (\text{S3.2})$$

with  $\mathbf{k} = (k_x, k_y)$ .  $|\psi_n^R(\mathbf{k})\rangle$  satisfies the eigen function

$$H(\mathbf{k})|\psi_n^R(\mathbf{k})\rangle = E_n(\mathbf{k})|\psi_n^R(\mathbf{k})\rangle. \quad (\text{S3.3})$$

Note that we only employ the right eigenstates. To perform the evaluation of Chern number effectively, we generalize the method from Ref. [96] using the lattice gauge theory, which is proved to be effective for the Hermitian case.

We first compute the eigen function of the Hamiltonian  $h(\mathbf{k})$  in Eq. (S2.2) on meshes in the Brillouin zone as follows

$$h(\mathbf{k}_j)|\varphi_n^R(\mathbf{k}_j)\rangle = \epsilon_n|\varphi_n^R(\mathbf{k}_j)\rangle, \quad (\text{S3.4})$$

where the momentum points are  $\mathbf{k}_j \equiv (j_x e_{k_x}, j_y e_{k_y})$  with  $e_{k_x} = \frac{2\pi}{qN_x}$  and  $e_{k_y} = \frac{2\pi}{N_y}$ . Here  $j_x(j_y)$  is an integer taking values from  $0, 1, 2, \dots, N_x(y) - 1$ . We define a  $U(1)$  link for each Hofstadter band as [96]

$$M_{n,\alpha=x,y}(\mathbf{k}_j) \equiv |\det U_{n,\alpha}(\mathbf{k}_j)|^{-1} \det U_{n,\alpha}(\mathbf{k}_j) \quad (\text{S3.5})$$

with the matrix

$$[U_{n,\alpha}(\mathbf{k}_j)]_{sp} = \langle \varphi_{n,s}^R(\mathbf{k}_j) | \varphi_{n,p}^R(\mathbf{k}_j + \hat{e}_\alpha) \rangle, \quad (1 \leq s, p \leq m), \quad (\text{S3.6})$$

where  $m$  is the number of states in the  $n$ -th non-Hermitian Hofstadter band. This link variables are well-defined except at singular points with  $\det U_\alpha(\mathbf{k}_j) = 0$ . The singularity indicates the existence of ‘‘vortices’’ or ‘‘anti-vortices’’ in the wave function. With this link variable, we obtain a lattice field strength as

$$F_{n,xy}(\mathbf{k}_j) \equiv \ln [M_{n,x}(\mathbf{k}_j)M_{n,y}(\mathbf{k}_j + \hat{e}_x)M_{n,x}^{-1}(\mathbf{k}_j + \hat{e}_y)M_{n,y}^{-1}(\mathbf{k}_j)]. \quad (\text{S3.7})$$

Finally, the Chern number on the lattice is given by

$$C_n = \frac{1}{2\pi i} \sum_j F_{n,xy}(\mathbf{k}_j). \quad (\text{S3.8})$$

This Chern number is proved to be an integer, as it counts the number of vortices minus the number of anti-vortices. It is numerically verified to be an integer in the non-Hermitian case considered here.

### Appendix S4: Evolution of the energy spectrum at small fields

In this section, we discuss the spectra of Eq. (S1.3) under small magnetic fields. Figure S4 presents the evolution of the bulk energy spectrum of a finite-size system as the magnetic field increases in the small field region. We find that the area of the bulk spectrum in the complex plane shrinks rapidly by increasing the magnetic flux. The sensitivity of the bulk spectrum against magnetic flux becomes more pronounced for a large system. Notice that a finite area in the bulk spectrum indicates the presence of the geometry-dependent FOSE [63]. The strong suppression of the spectrum area by magnetic fields indeed can reflect the magnetic suppression of the FOSE.

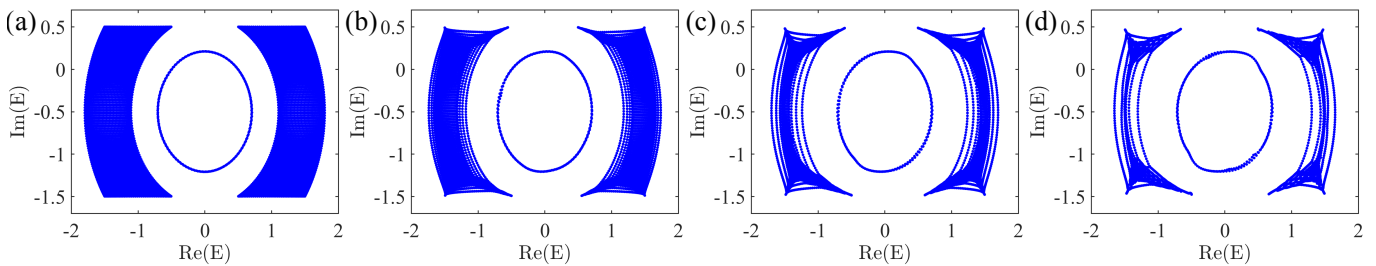


Fig. S4. Energy spectra on a square geometry under OBC for  $L_x = L_y = 100$  and increasing flux densities from  $\phi = 0$  (a),  $6\pi/1000$  (b),  $12\pi/1000$  (c) to  $20\pi/1000$  (d) (in units of  $h/e$ ). The area of the bulk spectrum in the complex energy plane shrinks rapidly by increasing the flux.

### Appendix S5: Edge spectrum of the models on a ribbon geometry

In this section, we demonstrate the existence of 1D edge modes of the considered models [cf. Eqs. (S1.3) and (S7.1)] on a ribbon geometry. For the minimal model in Eq. (S1.3), the bulk bands have zero Chern number at zero magnetic field. However, it exhibits 1D topological modes in a ribbon geometry, as shown in Fig. S5(a). These edge modes do not connect to the bulk bands directly but are also protected from a line-gap topology. They form a closed loop with a point gap in the complex energy plane. For the model in Eq. (S7.1), the bulk bands have nonzero Chern numbers in proper parameter regimes. Therefore, the chiral edge states connect the bulk bands, as shown in Fig. S5(b).

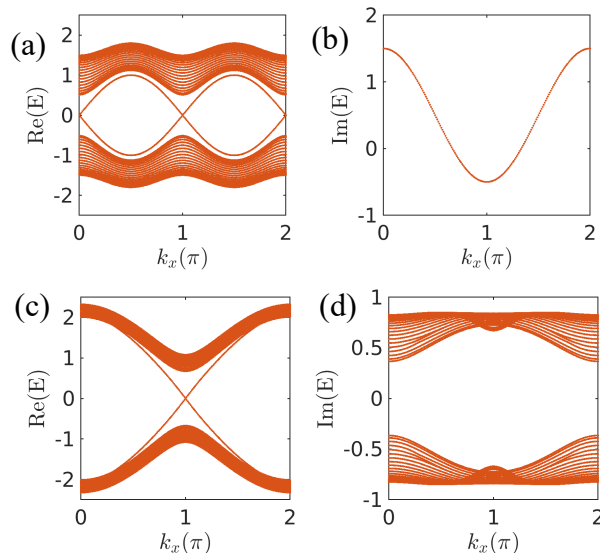


Fig. S5. (a) and (b) Real and imaginary energy spectra of Eq. (S1.3) on a ribbon geometry with partial OBC in  $x$ -direction while PBC in  $y$ -direction. (c) and (d) are the same as (a) and (b) but for the model in Eq. (S7.1). For (a) and (b), the parameters are  $\gamma = 0.5$  and  $\lambda = 1$ . For (c) and (d), parameters are  $\gamma_x = t = 1$ ,  $\gamma_y = 0.2$  and  $\delta = 0.6$ .

### Appendix S6: SOSE model with point gap topology

In this section, we study the model [cf. Eq. (3) in the main text] for the SOSE with point-gap topology. The model has a hybrid skin effect at zero field, showing both FOSE and SOSE simultaneously. The OBC spectrum consists of  $\mathcal{O}(L)$  modes in the spectral area of the PBC point gaps, as well as  $\mathcal{O}(L^2)$  “bulk” modes outside these point gap areas [see Fig. S6(a) for the OBC spectrum]. The hybrid topology is characterized by the fact that not only the eigenenergy modes in the nontrivial energy regions [within the dashed circles in Fig. S6(a)], but also extensive continuum ones (outside the dashed circles) tend to localize at the corners of the systems under OBC. We confirm this numerically in

Fig. S6(b)-(d).

In Fig. S7(a), we calculate the scaling exponent  $\alpha = d\log(w_{sc})/d\log(L)$  for different  $L$  and  $\xi$ . We find that  $\alpha$  is always significantly larger than 1 (the value for the pure SOSE) and it increases as  $L$  grows. This further supports the hybrid skin effect in the system. In Fig. S7(b), we calculate the skin corner weight  $w_{SC}$  as a function of  $L$  for increasing magnetic field. We find that the scaling behavior of  $w_{sc}$  with respect to  $L$  takes a curved line at zero field, while it becomes a nearly straight line at strong fields (i.e.,  $Ba^2 > 0.05\pi$ ).

Finally, we present the spectra of the model under magnetic fields. Without magnetic fields, the model has skin corner modes under OBC [Fig. S8(a)]. When considering strong magnetic effects, the PBC spectrum splits to multiple non-Hermitian Hofstadter bands [Fig. S8(b)]. These bands carry non-zero Chern numbers, which can be calculated similarly as that in the previous section (Sec. (S3)). Saliiently, we also find that fractal structures appear in both the real and imaginary Hofstadter spectra [Figs. S8(c) and S8(d)]. At small fields, it shows the formation of Landau levels. It is also worthy noting that line gaps quickly develop when applying a magnetic field, as shown in Fig. S8(d).

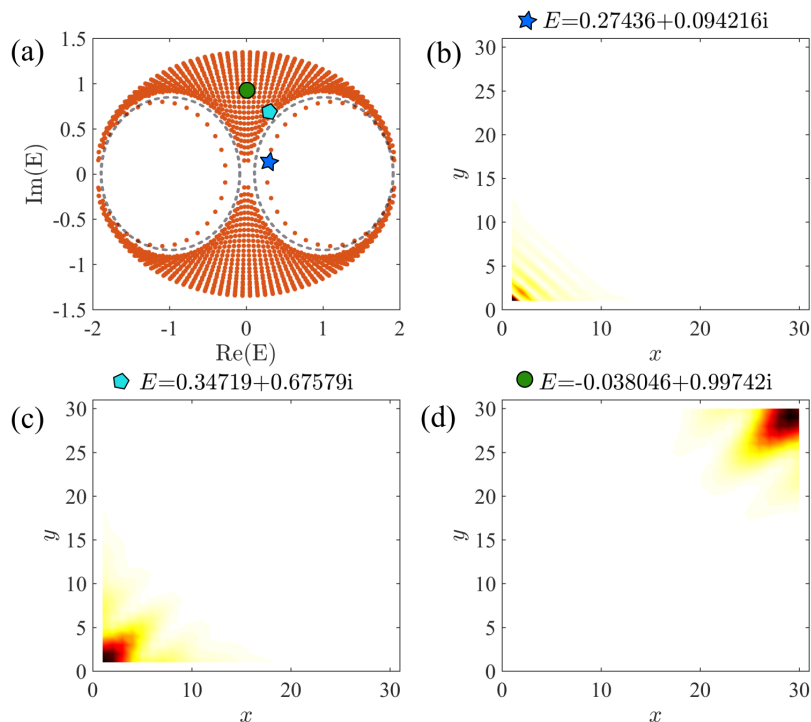


Fig. S6. Energy spectrum under full OBC at zero field. The modes with energies inside the dashed circles resemble the skin corner modes associated with intrinsic second-order topology (point gaps in the bulk spectrum). (b) Wavefunction distribution  $|\psi^R|^2$  of a mode with energy inside the circles [indicated by the dark blue star in (a)]. (c) and (d) are the same as (b) but for two modes outside the circles (indicated by the cyan pentagon and green disk, respectively). Other parameters are the same as Fig. 4 in the main text.

### Appendix S7: Generalization to other models with SOSE

In this section, we generalize our result to another model of the SOSE with line gap. We have shown that the SOSE is robust and can even be enhanced under magnetic fields. To better support the generality and experimental feasibility of our theory, we further consider a different model with the SOSE [73, 81]

$$\begin{aligned}
 H_2(\mathbf{k}) = & (\gamma_x + t \cos k_x)\tau_1\sigma_0 - t \sin k_x\tau_2\sigma_3 + i\delta\tau_1\sigma_2 \\
 & - (\gamma_y + t \cos k_y)\tau_2\sigma_2 - t \sin k_y\tau_2\sigma_1 - i\delta\tau_2\sigma_0,
 \end{aligned} \tag{S7.1}$$

where  $\sigma_i$  and  $\tau_i$  ( $i = 1, 2, 3$ ) are Pauli matrices for the four sublattice degrees of freedom in a unit cell.  $t$  is the strength of intercell hopping, and  $\gamma_{x/y} \pm \delta$  the nonreciprocal hopping amplitudes occurring within unit cells in  $x/y$ -directions. Note that this model has been realized experimentally [80]. For  $|\gamma_x| < t$  (or  $|\gamma_y| < t$ ) and  $|\delta| > 0$ , the model shows

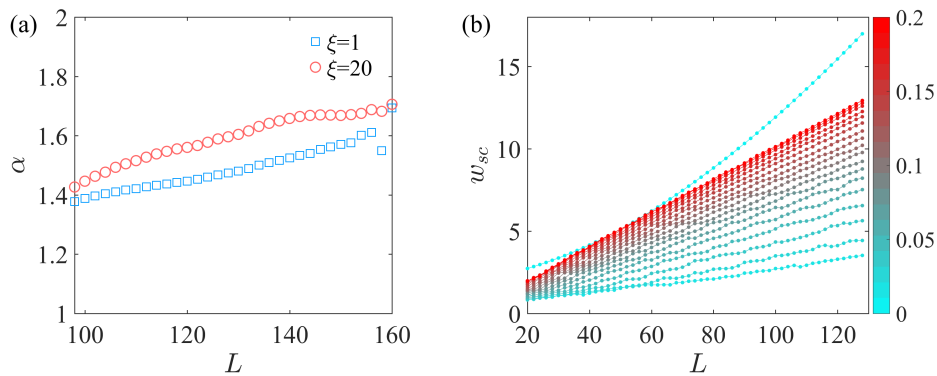


Fig. S7. (a) Scaling exponent  $\alpha = d \log(w_{sc})/d \log(L)$  as a function of system size  $L$ . (b) Skin corner weight  $w_{sc}$  as a function of  $L$  for increasing  $Ba^2$  from 0 (cyan) to  $0.02\pi$  (red). Parameters:  $\xi = 1$  in (b), and other parameters are the same as Fig. 4 in the main text.

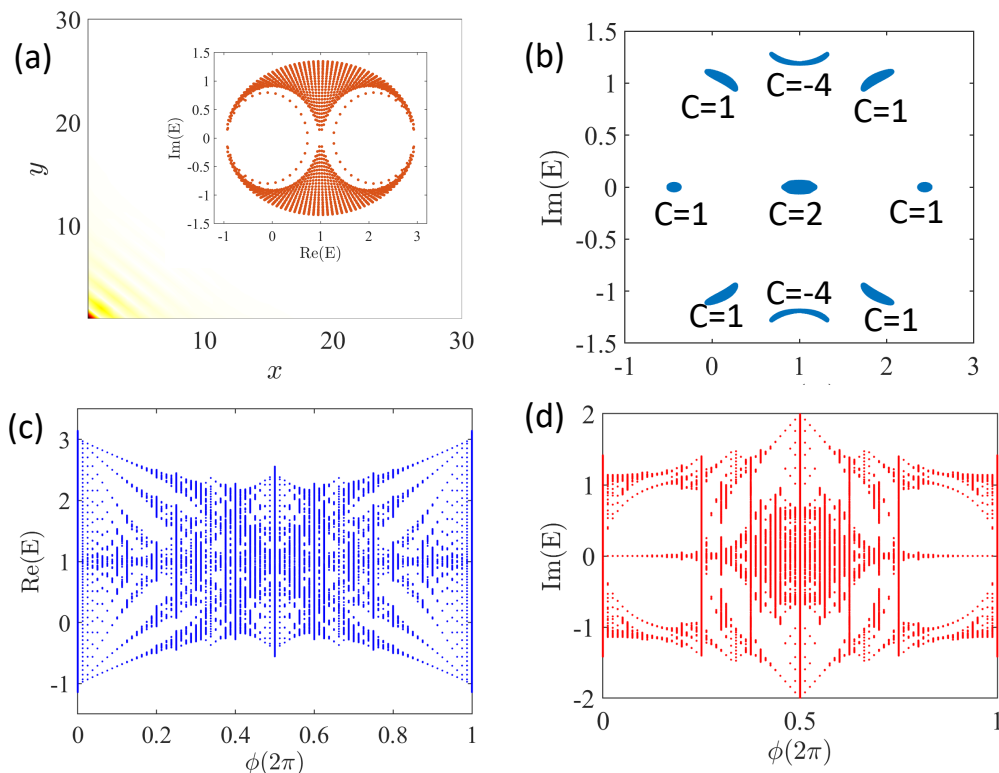


Fig. S8. (a) Energy spectrum at zero field (inset) under OBC and distribution  $|\psi^R(\mathbf{r})|^2$  of a skin corner mode with energy  $E = 1.27 + 0.09i$ . (b) Non-Hermitian Hofstadter bands at  $Ba^2 = 0.4\pi$  under PBC. The numbers  $C$  stand for the Chern numbers of the bands. Real (c) and imaginary (d) parts of energy spectrum under PBC as a function of magnetic flux  $\phi = Ba^2$ . Other parameters are the same as Fig. 4 in the main text.

the SOSE, which can be understood similarly based on edge modes. The FOSE is prohibited by the presence of two transpose-mirror symmetries, similar to the minimal model in the main text. However, the edge modes in this model are chiral-like and appear when OBC are imposed to either direction, different from the minimal model. For  $|\gamma_x| > t$  and  $|\gamma_y| > t$ , the SOSE is absent in the model at  $B = 0$  for any  $\delta$ .

Using the formula of skin corner weight defined in the main text, we calculate  $w_{sc}$  of the model in Eq. (S7.1) under OBC as increasing magnetic field  $B$ . For illustration, we consider  $\gamma_x = t = 1$  and  $\delta = 0.6$  and present  $w_{sc}/L$  as a function of  $B$  for different  $\gamma_y$  [Figs. S9(a) and (b)]. At  $B = 0$ ,  $w_{sc}/L$  is vanishingly small for large  $\gamma_y (> t)$ ,

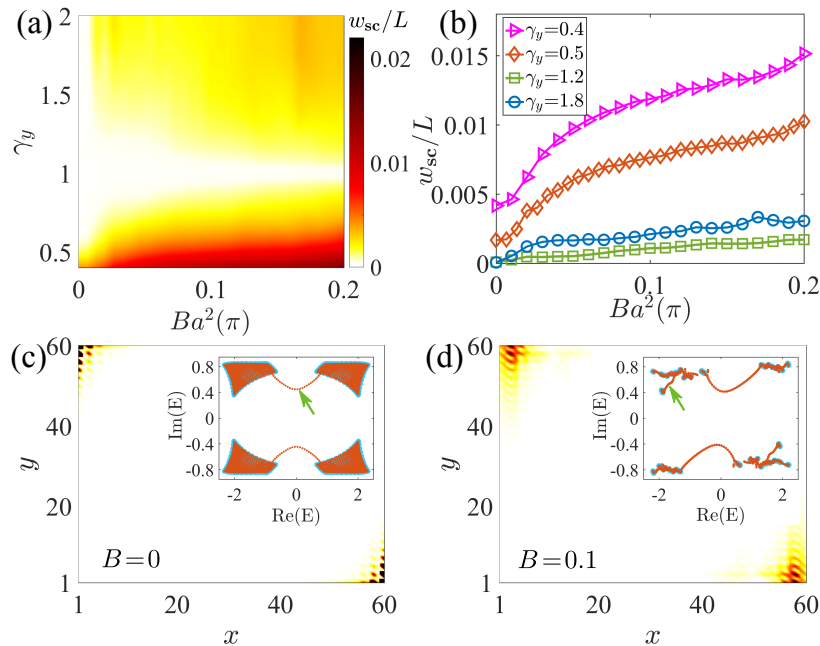


Fig. S9. (a)  $w_{sc}/L$  as a function of  $B$  and  $\gamma_y$ . (b)  $w_{sc}/L$  as a function of  $B$  for different  $\gamma_y$ . (c)  $|\psi^R(\mathbf{r})|^2$  of a skin corner mode at  $B = 0$  under OBC. Inset: the PBC (cyan) and OBC (orange) energy spectra. The arrow marks the mode energy  $E = 0.04 - 0.45i$ . (d) the same as (a) but for  $Ba^2 = 0.1\pi$ . The arrow marks the mode energy  $E = -1.73 + 0.49i$ . Other parameters:  $\gamma_x = t = 1$ ,  $\gamma_y = 0.2$ ,  $\delta = 0.6$  and  $L = 60$ .

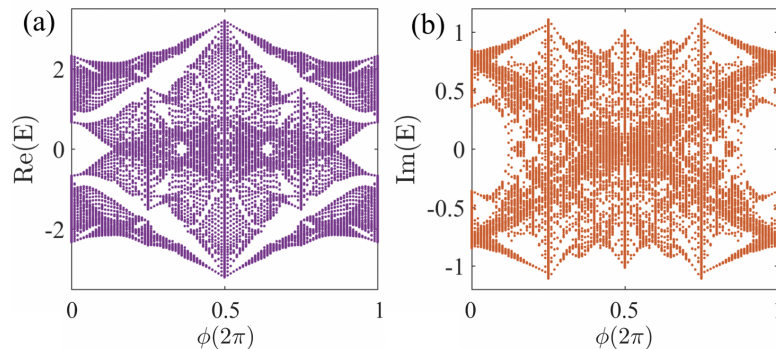


Fig. S10. Real (a) and imaginary (b) parts of energy spectrum as a function of magnetic flux  $\phi = Ba^2$  under PBC. Other parameters:  $\gamma_x = t = 1$ ,  $\gamma_y = 0.2$ ,  $\delta = 0.6$ .

whereas it becomes considerable for small  $\gamma_y (< t)$ . This confirms the absence (presence) of the SOSE for  $\gamma_y > t$  ( $\gamma_y < t$ ). Evidently,  $w_{sc}$  increases significantly under  $B$  for proper parameters. These features clearly demonstrate the enhancement (for  $\gamma_y < t$ ) and emergence (for  $\gamma_y > t$ ) of SOSE by magnetic fields. We can also find that the SOSE is ultimately related to the formation of topological line gaps in the bulk spectrum under  $B$ , as shown in Fig. S9(d).

We further plot the real and imaginary parts of the spectrum of the model in Eq. (S7.1) as a function of magnetic flux in Figs. S10(a) and (b), respectively. Both spectra exhibit Hofstadter's fractal-like structures independently. We argue here that the major difference lies in rich internal degrees of freedom in our considered model Eq. (S7.1). We also note the persistence and emergence of topological line gaps, which accounts for the anomalous magnetic robust behaviors discussed above.

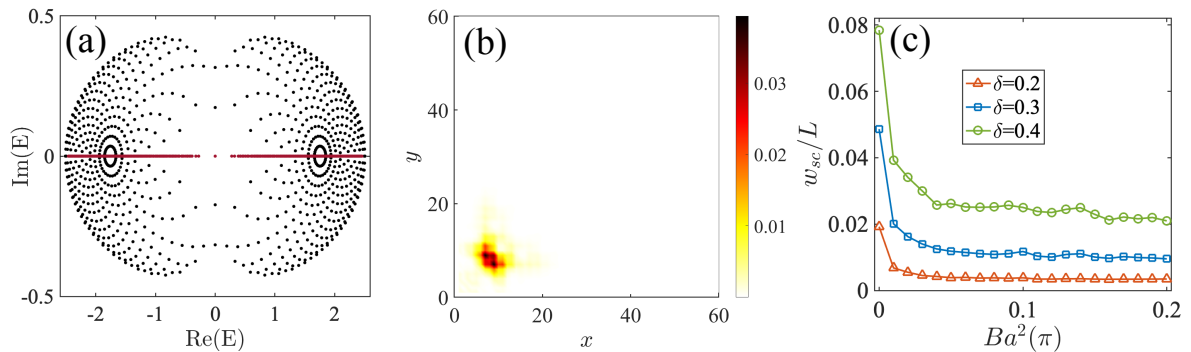


Fig. S11. Magnetic suppression of the first-order skin corner modes. (a) Energy spectra for the PBC (black) and the OBC (red), respectively. (b) Wavefunction  $|\psi^R(\mathbf{r})|^2$  of an eigenenergy state with energy  $E = -0.6$  at  $Ba^2 = \pi/10$ . The state is moved away from the corner by the magnetic field  $B$ . (c)  $w_{sc}$  as a function of  $B$  for different nonreciprocal strengths  $\delta$ . Other parameters are  $\gamma_x = \gamma_y = 0.8$ ,  $\lambda = 1$  and  $L = 60$  in all panels, and  $\delta = 0.3$  in (a) and (b).

### Appendix S8: Magnetic suppression of the first-order skin effect

In this section, we show the magnetic suppression of the FOSE. The FOSE may also exhibit skin corner modes. We demonstrate here that the magnetic field will significantly suppress the skin corner modes arising from the first-order nature, rather than showing magnetic robustness or enhancement. To illustrate this point explicitly, we consider the following model [34]

$$H_{1st}(\mathbf{k}) = (\gamma_x + \lambda \cos k_x)\tau_1\sigma_0 - (\lambda \sin k_x + i\delta)\tau_2\sigma_3 - (\gamma_y + \lambda \cos k_y)\tau_2\sigma_2 - (\lambda \sin k_y + i\delta)\tau_2\sigma_1, \quad (\text{S8.1})$$

where  $\sigma_i$  and  $\tau_i$  ( $i = 1, 2, 3$ ) are Pauli matrices for the four sublattice degrees of freedom in a unit cell. The nonreciprocal hopping occurs in both  $x$ - and  $y$ -directions with the corresponding hopping amplitudes  $\gamma_{x/y} \pm \delta$ . This model exhibits skin corner modes but whose number scales with the area of the system  $L^2$  in 2D, which is of FOSE by definition. In contrast to the models of the SOSE, the nonreciprocal hoppings in Eq. (S8.1) are finite throughout the system. An effective nonreciprocal vector in the bulk can be found, which points in [11] direction. Note that the model reduces to the Benalcazar-Bernevig-Hughes model in the Hermitian limit of  $\delta = 0$  [105? ].

As shown in Fig. S11(a), the energy spectrum of the model under OBC is dramatically different from that under full PBC: the PBC spectrum (for  $L \rightarrow \infty$ ) covers a finite area with point-gap topology in the complex-energy plane, while the OBC spectrum forms two separated lines on the real axis (under chosen parameters). Under OBC, we observe that all eigenstates of the system are localized to the left-bottom corner, forming skin corner modes. When applying a magnetic field, we find that an extensive number of corner states are pushed away from corners due to the strong magnetic confinement effect and the breakdown of point-gap protection [86] [see Fig. S11(b) for an illustration]. We again employ the previously defined skin corner weight  $w_{sc}$  to characterize the magnetic response in present case. Such a suppression of the first-order skin corner modes is clearly indicated by the obvious decrease of  $w_{sc}$  as increasing magnetic field strength [Fig. S11(c)]. This result clearly distinguishes the magnetic response of the FOSE from the second-order one and reveals their different topological properties.

### Appendix S9: Magnetic robustness of the third-order skin effect

In this section, we discuss the magnetic response of the third-order skin effect. To be specific, we consider the prototypical model [72]

$$H_{3rd} = i\lambda \sin k_y \sigma_x + i(\gamma + \lambda \cos k_y) \sigma_y + i\lambda \sin k_x \sigma_z + (\gamma + \lambda \cos k_x) \tau_z + \lambda \sin k_z \tau_y + (\gamma + \lambda \cos k_z) \tau_x, \quad (\text{S9.1})$$

where  $\sigma$  and  $\tau$  are Pauli matrices in sublattice spaces,  $\gamma$  and  $\lambda$  are real parameters. Under OBC, there are  $\mathcal{O}(L)$  skin corner modes emerge in all  $\mathcal{O}(L^3)$  modes, as shown in Fig. S12(a). When applying a magnetic field, we find that the



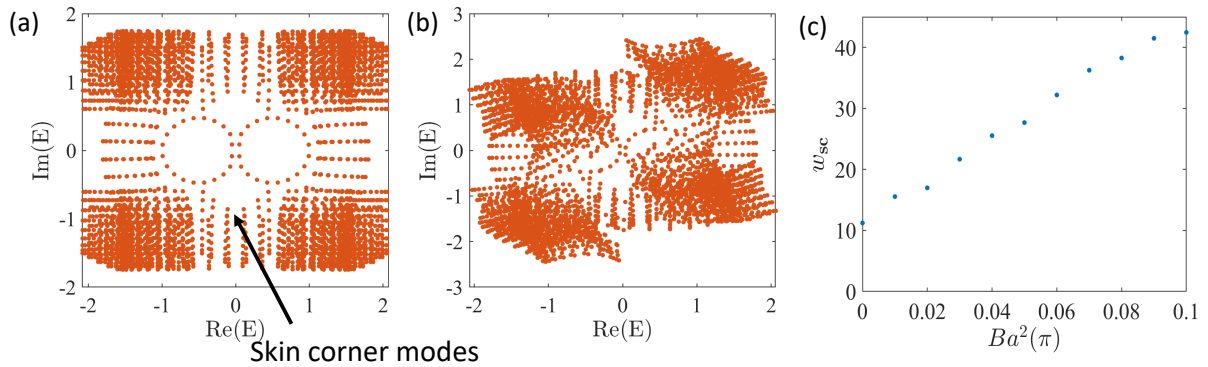


Fig. S12. OBC energy spectrum of the model in Eq. (S9.1) with the third-order skin effect at  $Ba^2 = 0$  (a) and  $0.04\pi$  (b). (c) Skin corner weight as a function of  $Ba^2$ . Other parameters:  $\lambda = 1$ ,  $\gamma = 0.5$ ,  $L = 10$ .

skin corner modes survive in the line gap [Fig. S12(b)]. Similarly, we define the skin corner weight as

$$w_{sc} = \sum_{n, \mathbf{r}, \mathbf{r}_c} |\psi_n^R(\mathbf{r})|^4 \exp(-|\mathbf{r} - \mathbf{r}_c|/\xi), \quad (\text{S9.2})$$

similar to the 2D case, in which all eight corners are taken into account. Figure S12(c) plots  $w_{sc}$  as a function of magnetic field  $B$ . We see that  $w_{sc}$  increases significantly as  $B$  increases. Thus, we conclude the magnetic robustness and enhancement of the third-order skin effect. The underlying mechanism is similar to that of the SOSE with line gaps.